Chapter 4

BREAKING UP: IN-SITU FRACTURE EXPERIMENTS PERFORMED ON POLYCRYSTALLINE ALUMINUM OXYNITRIDE

Sections of this chapter were previously published in: **Gorske, S.F.**, Park, J-S., Kenesei, P., Sharma, H., Almer, J., Voorhees, P., Faber, K.T. "In-situ visualization of a growing brittle crack in aluminum oxynitride using synchrotron X-rays and the double-cleavage drilled compression geometry". *Acta Materialia*, vol. 312, 2026, 122213. https://doi.org/10.1016/j.actamat.2026.122213

4.1 Introduction

When a crack grows through a fully dense, polycrystalline material, the orientations of the constituent grains have a significant impact on quantities like fracture toughness and stress-strain response [1–4]. Additionally, the grain boundaries will have a fracture toughness of their own. Altogether, this means that the energetic description of the material's interior is much more complex than in an isotropic material or matrix, such that predicting where the energy of the crack will be minimized as it grows is difficult, as is understanding what factors impacted crack growth during its lifetime. While sequential focused-ion beam studies on fractured polycrystalline materials can bear some indication of where a crack grew transgranularly (through a grain) or intergranularly (around a grain on a grain boundary), the local strain within grains and the velocity of the crack on or off particular slip planes is largely unknown.

Outside of brittle materials, synchrotron studies of polycrystalline metals undergoing fatigue fracture have allowed for three-dimensional mapping of a crack and its relationship with grains over many loading states and crack lengths [5–10]. Studies of this type have elucidated crack tip phenomena, such as the differing stresses required for the crack to intersect grains at certain orientations and the pathways it might take along certain slip planes within that grain, as well as when intergranular fracture along grain boundaries may be energetically preferred [11–13]. As the crack interacts with grain boundaries and changing crystallographic orientation, the fracture toughness will consequently deviate from the numerically modeled and experimentally calculated average.

Aluminum oxynitride (AlON, $Al_{23-X/3}O_{27+X}N_{5-x}$) is a polycrystalline ceramic chosen for these experiments [14,15]. As a material with properties useful to industrial and military applications including optics and impact defense, understanding its crack propagation is relevant to many fields. Its equiaxed grains can be grown to be much larger than the crack tip radius, the crack opening width, and the synchrotron techniques' voxel resolution, but smaller by an order of magnitude or more than the DCDC sample's dimensions, such that the crack is bound to encounter grains from a variety of impingement angles and distances from the nearest grain boundary. It is also a face-centered cubic material, so its high crystal symmetry limits the span of orientations each grain can take, allowing for greater ease of computation and comparison. Crucially, the AlON under study also has extremely low porosity, allowing us to investigate its bulk fracture behavior. Two samples will be investigated in this study, demonstrating how changes in the microstructure from sample to sample are a major effect in crack growth.

4.2 Materials and Methods

4.2.1 Materials

AlON pieces were sourced from and machined within 0.2 mm accuracy into bars of dimensions $1.4 \times 1.4 \times 16$ mm^3 by Surmet Corporation (Figure 4.1a). The cross-sectional diagonal was therefore under 2 mm and fits within the synchrotron beam width of 2.1 mm, obviating the need for stitching of tomographic volumes to cover the entire sample cross-section. The drilled holes had surface diameter of 0.42 mm (Figure 4.1b) and deviated from the ideal DCDC geometry, as the holes narrowed conically toward the center of the sample (Figure 4.1c). Additionally, the edges of the faces in contact with the compression platens were lightly chamfered using 1200-grit SiC grinding media to eliminate any unevenness. Two samples, termed Sample 1 and Sample 4 upon receipt from Surmet, were tested. These samples were selected randomly from the number provided; Samples 2 and 3 were not tested. The majority of the grains in both samples were equiaxed and had radii in the range of 50-150 μm, distributed uniformly throughout the volume.

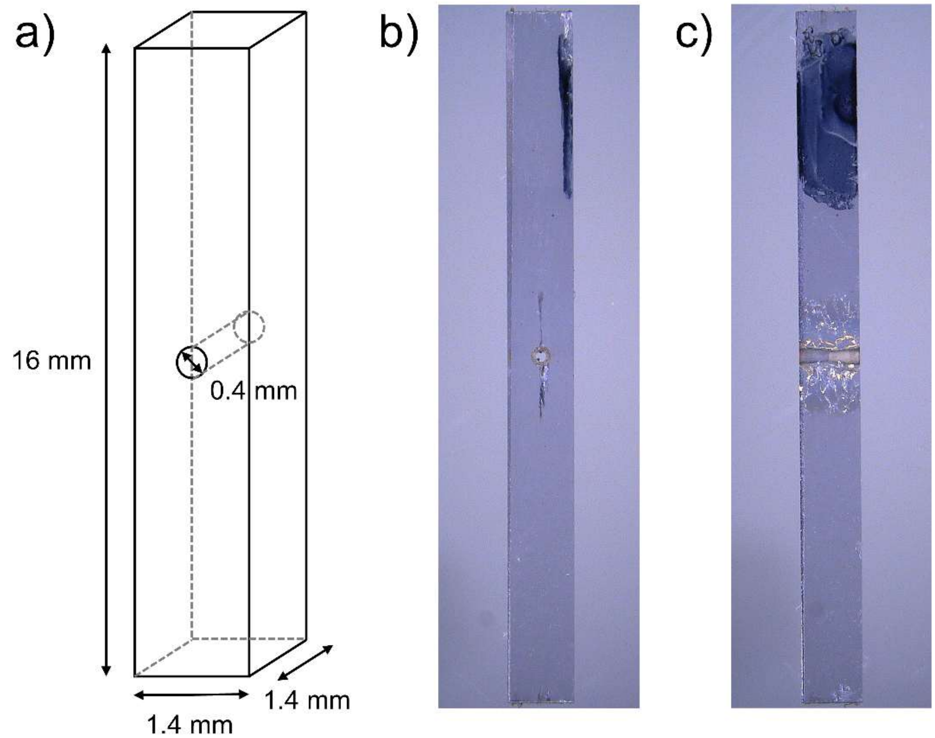

Figure 4.1: The double-cleavage drilled compression geometry. a) Schematic with dimensions used in this experiment b-c) post-experiment optical micrographs of Sample 1 showing the shape and location of the crack, via projections respectively parallel to and perpendicular to the drilled hole; black Sharpie indicates the side investigated during the experiment.

4.2.2 Methods

Synchrotron measurements were performed at the 1-ID beamline of the Advanced Photon Source (APS) at Argonne National Laboratory (ANL). For all measurements, the X-ray beam was tuned to the Hf K-edge (energy of 65.351 keV, wavelength of 0.18971 Å, bandwidth $\Delta E/E \sim 10^{-3}$).

4.2.2.1 Loading

Samples were compressed using the 3rd-generation Rotational and Axial Motion System (RAMS-III) designed by Shade et al. at the Air Force Research Laboratory [16]. A set of steel platens of area 3.2 mm x 3.2 mm were used. In this setup, the maximum allowable compression loading limit was -2 kN. The reference frame for measurements is depicted in

Figure 4.2, where *y* is the loading direction, *z* is directed along the beam, *x* is orthogonal to *y* and *z*, and RAMS-III is rotated about the *y* direction. The sample was mounted and aligned using radiography to ensure its central axis coincided with the loading (*y*) direction. Loading was manually controlled in displacement mode with steps of 0.2 μm, roughly every 2 seconds; displacement at this scale was crucial to prevent large displacement changes, correlating to large increases in load which might lead to catastrophic failure. A live radiograph of the sample, aligned so that the beam was parallel to the hole direction, was monitored to watch for signs of crack pop-in or extension. Whenever this happened, or when the sample load magnitude decreased upon further compression, loading was stopped. The magnitude of the applied load was then manually decreased by 50-100 N to prevent further extension during X-ray measurements, then the load frame was switched over to load control as scanning and rotation commenced.

4.2.2.2 FF-HEDM

FF-HEDM measurements were taken with a single panel GE 41RT amorphous-Si detector (2048 x 2048 pixels, 0.2 mm/pixel) located 1.4 m downstream from the sample (Figure 4.2a). A box beam of dimensions 2.1 mm (*x*) x 0.1 mm (*y*) was used for all volumes probed. Diffraction patterns were recorded 360° in ω with frames in intervals of $\Delta\omega$=0.25° for a total of 1440 frames per scan. The Microstructure Imaging for Diffraction Analysis Software (MIDAS) was used to identify the orientation, center of mass (COM), size, and elastic strain tensor (ε) of the constituent grains in the illuminated volume [17-19]. Diffraction spots from the {311}, {400}, {422}, {511}, and {440} peaks were present in sufficient number and intensity to be used for characterization of individual grains. When the ratio of number of observed diffraction spots to the theoretical number present in a complete Bragg pattern for that orientation (termed completeness) exceeded 80%, the grain was retained for further analysis. The anisotropic cubic stiffness tensor of a single AlON crystal (C_{11} = 334.8 GPa, C_{12} = 164.4 GPa, C_{44} = 178.6 GPa [20]) was used to generate the stress tensors from the corresponding strain tensors.

FF-HEDM scans at near-zero load were used to calculate the unstrained lattice parameter. The grains in Sample 1 had a mean lattice parameter of 7.9486 Å at -5 N load and those in Sample 4 had a value of 7.9461 Å at -30 N load. Both values are within Surmet's reported range of lattice parameters for AlON, which can vary depending on the ratio of oxygen to nitrogen in its formula [14], so this difference in lattice parameters ($\Delta a/a \sim 2 \times 10^{-4}$) is unsurprising for two samples from different batches. Using the average lattice parameter between these two samples as a baseline resulted in the estimated residual stress at zero load to be on the order of ±100 MPa in all directions, so the strains in each sample were computed using their respective values for the unloaded lattice parameter a0.

4.2.2.3 NF-HEDM

NF-HEDM measurements were taken with an in-house designed detector (2048 x 2048 pixels, 1.48 mm/pixel) with a QImage Retiga 4000DC CCD camera positioned sequentially at two distances, 8.56 mm and 11.56 mm away from the center of the sample, and a focused beam 1 µm (y) x 2 mm (x) [21,22] (Figure 4.2b). For each scan, the sample was rotated 180° with $\Delta\omega$=0.25°, generating 720 diffraction images per detector distance. The scans were spaced µm apart so as to cover a larger volume; between scans, the grain boundaries can be reasonably interpolated due to the much larger relative size of the AlON grains. The MIDAS software was also used to process the data; using the grain orientations from the corresponding far-field scans as a seed, the software assigned each 5 x 5 x 5 µm^3 voxel a most-likely orientation and a confidence value.

4.2.2.4 µ-CT

The µ-CT measurements were taken with an in-house designed detector (1920 x 1200 pixels, 1.172 mm/pixel) which utilized a PointGrey Grasshopper3 CMOS camera (Figure 4.2c). The beam was 2.1 mm x 1 mm, and radiographs were acquired at 0.2° $\Delta\omega$ steps from 0 to 360° with 0.077 s exposure for 1800 total frames. Ten bright-field images and ten dark-field images were acquired for normalization. In-house software was then used to reconstruct the volume with the GRIDREC algorithm implemented in MIDAS [23] resulting in a tiff image with 1024 layers and voxel size 1.17 x 1.17 x 1.17 µm^3. Features with dimensions greater than 5 µm in a given direction could be clearly rendered, with smaller features becoming semi-visible until they were smaller than the voxel size.

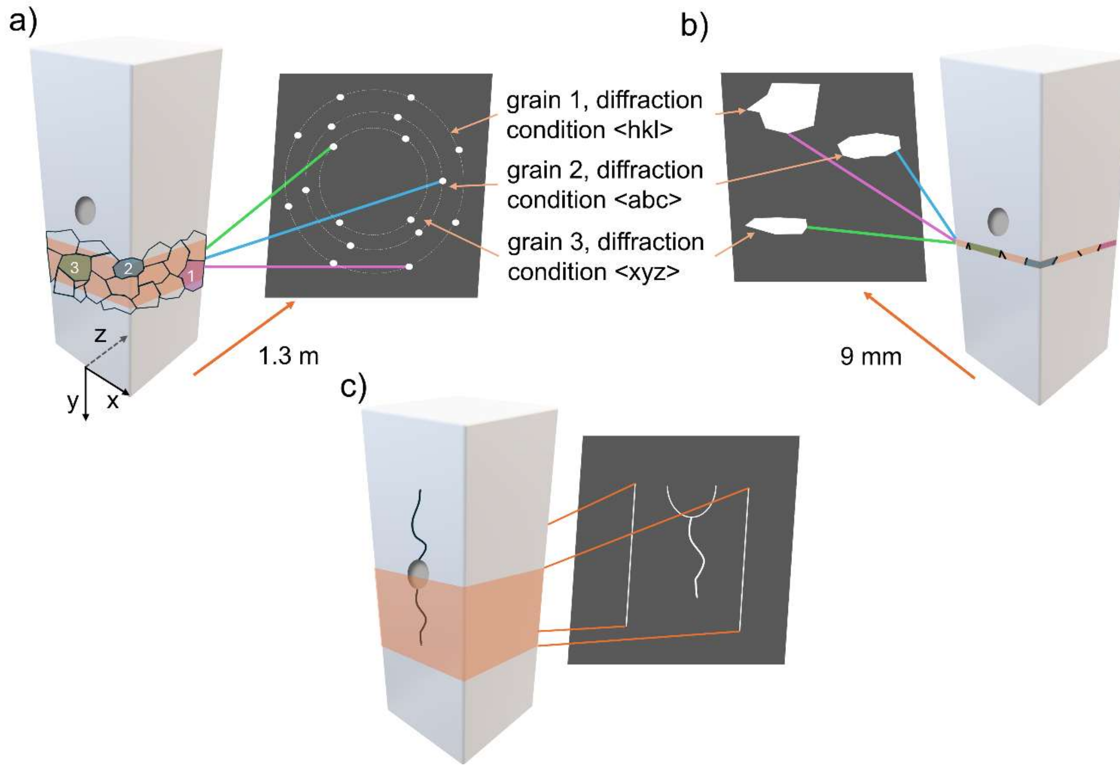

Figure 4.2: Visualization of synchrotron X-ray HEDM and μ-CT performed at Beamline 1-ID with frame directions: a) FF-HEDM, with reference frame marked. b) NF-HEDM. c) μ-CT.

4.2.2.4.1 Crack detection program

Post-processing of the tomography images started with the application of a non-local means filter [24] throughout the entire volume, with the region size chosen automatically by the ImageJ software, to decrease background noise. Next, a median filter extending two pixels in each direction away from the central voxel was applied for further smoothing and suppression of any remaining ring artifacts. Finally, a second non-local means filter was applied to each layer of the image stack individually, without input from the rest of the volume. After these steps, a custom crack detection program was used to determine the location and width of the crack structure as well as the approximate location and error bounds of the crack tip.

The first part of the program used slices of the tomographic volume perpendicular to the direction of loading, specified as the y-axis. Figure 4.3 displays representative slices of studied AlON samples with the coordinate system labeled. The primary method of detecting the crack was marking locations on the 2D slice where, along a 1D intensity line, a sinusoidal shift in intensity marked a phase change (in this case, air to solid and vice versa). As air absorbs fewer X-rays than a solid, a drop in image intensity corresponds to a decrease in absorption, and thus the potential presence of a crack. Because of the phase contrast, the intensity should also peak above the background before the phase change, creating the sinusoid-like intensity profile. The clearest indication of a crack is when an intensity drop (defined as 125% of the standard deviation below the mean after testing multiple values) is bounded on either side by an intensity peak (75% of the standard deviation above the mean), representing the double phase-change from solid to air and back. In order not to exclude features that did not exactly meet these criteria, two additional markers deviating from ideal were included in the algorithm: a single peak beside a 150% standard deviation absorption drop, as well as a 200% standard deviation decrease in intensity without any peaks. Further, the crack opening behind the crack front was at maximum less than ten pixels, or 11.7 μm wide, and grew narrower closer to the crack tip. As a result, the distance between the two phase changes grew increasingly smaller and the two sinusoids could be indistinguishable. Thus, locations lacking an intensity drop and only possessing an intensity peak can also indicate the presence of the crack. However, since some bright artifacts were also present, as well as the peaks to either side of the already-marked crack locations, bright sections were only included in the crack pixel count when directly below previously marked crack spots.

After identifying these features, further filtering was implemented to reduce the presence of both false negatives and false positives. First, points identified as possibly belonging within the crack via the previous procedure were assigned to groups with the same (x,z) pixel location in different slices in the stack and sorted by height (y) within the tomographic volume, then the distance between consecutive marked points was computed. If fewer than one-third of the slices between the lowest and highest y-slice at that location contained an identified point, or if those slices were separated by less than 5 pixels, the location was considered spurious due to excess noise, and all points were removed from consideration as being part of the crack front. For locations with sufficient density of marked points, any gaps smaller than 10 pixels were deemed to be false negatives and filled in as part of the crack front. If the gap was larger, the marked locations on either side were treated as individual crack segments and subjected to the earlier considerations. By applying these arguments, an additional benefit was gained: the appearance of the crack front became self-similar for differing threshold values during the initial marking algorithm, thus eliminating much of the subjective nature of those values. Figure 4.4 displays the same tomographic slices as Figure 4.3 with the identified crack marked in blue.

4.2.2.4.2 Uncertainty in the crack length

Due to the narrow nature of brittle cracks, the singularity at the crack tip, and the limits of the tomographic resolution, the true extent of the crack tip is not visible directly in the tomography images. It was estimated by assuming the crack to narrow parabolically toward the crack tip [25] and measuring the crack width in a region until the resolution limit blurred the feature's existence; this occurred at around 3 pixels or 3.5 μm wide. Even at wider locations, the true width could be obscured by the presence of the phase-contrast wrinkle artifacts [26], so the measured width at every depth was not used in the calculation. Instead, the deepest point at which the crack had a specific width was used to fit the parabola (Figure 4.5), since even with uncertainty the crack never became that width again, indicating that it was indeed narrowing. The resultant parabola indicated that the true crack tip was 45-60 μm ahead of the final point used in fitting the curve. This roughly corresponded to the depth at which the crack detection program described in Section 2.2.4.1 identified the crack's presence. Further assuming that the crack could be up to 1 μm wider than measured due to the pixel resolution being much larger than the crack width near the tip showed that if this is the case, the crack tip could be up to 30 μm further ahead of the point identified by the crack detection program. The uncertainty in the depth of the crack tip as used in Equation 2.5 and Figure 4.4 was thus set to be 50 μm shorter than measured, indicating the distance from the last detected point to the last point with good resolution, to 25 μm longer than measured, the approximate distance that the crack tip might be away from the last detected point.

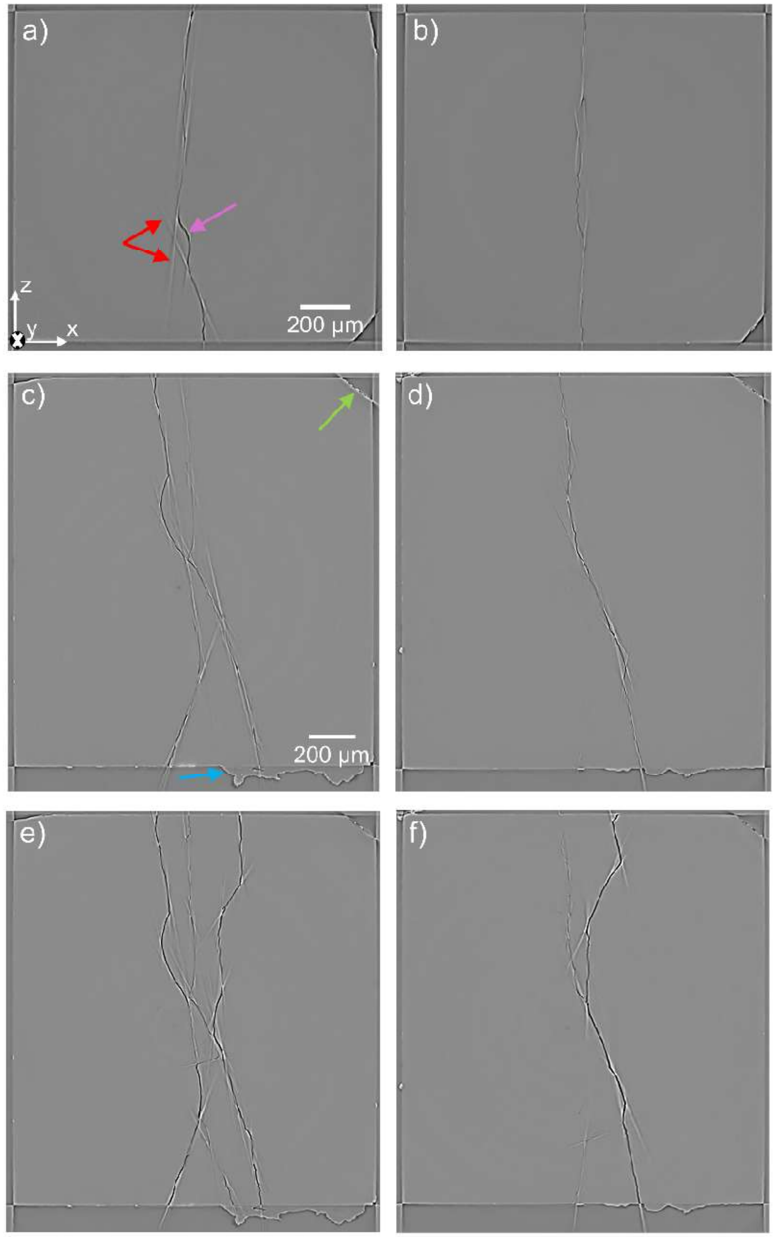

Figure 4.3: 2D crack trace in aluminum oxynitride viewed with μ-CT, where the loading direction y points into the page. Example features of note are marked, including the crack (purple), artifacts (red), machining errors (green), and debris from laser-cutting the hole (blue). a,b) The crack directly below the hole and 386 μm away from the hole, respectively, in Sample 1 at -1900 N. c) The crack directly below the hole in Sample 4 at -1450 N. d) The crack directly below the hole in Sample 4 at -1750 N. e) The crack 397 μm away from the hole in Sample 4 at -1450 N. f) The crack 394 μm away from the hole in Sample 4 at -1750 N.

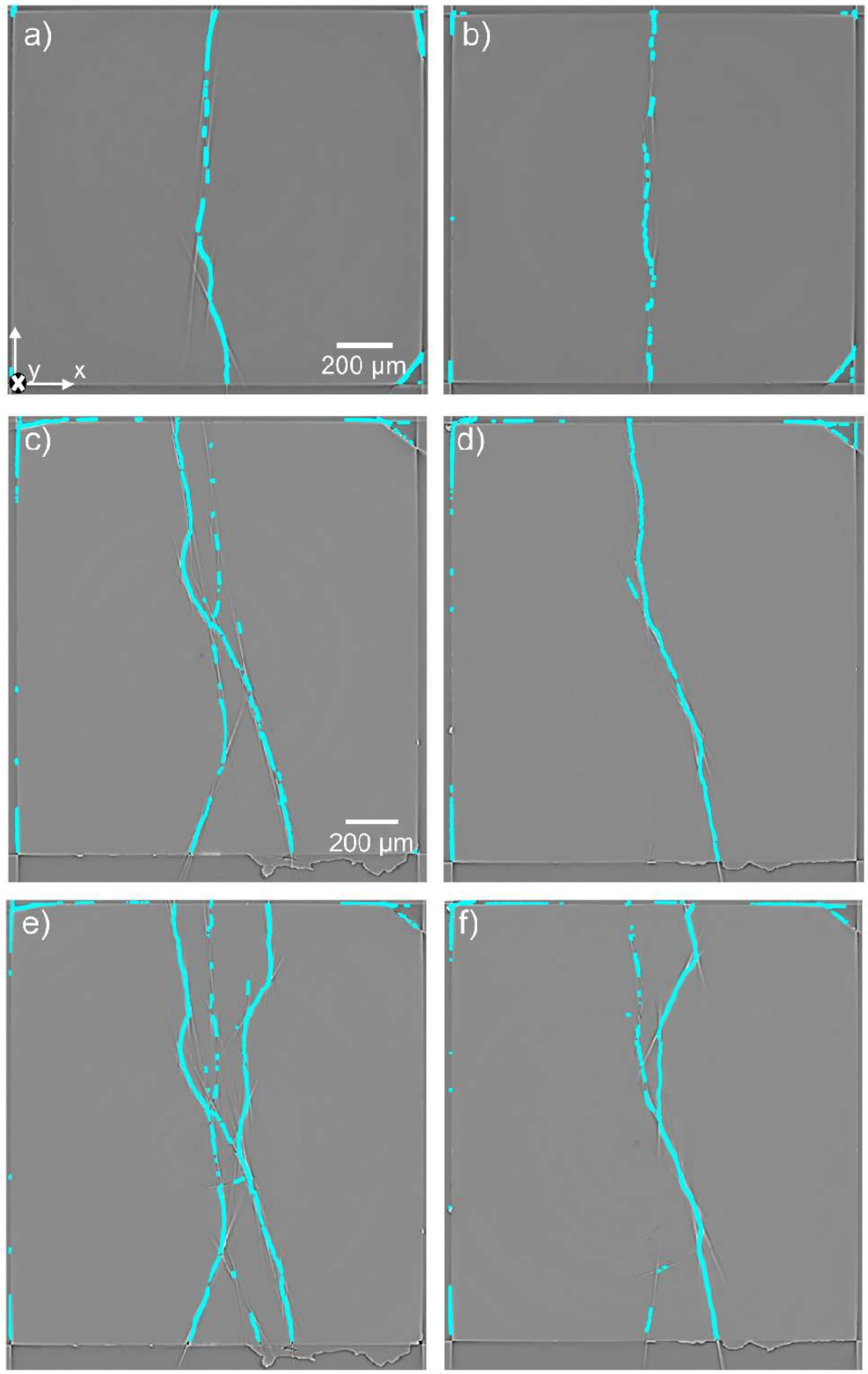

Figure 4.4: The crack detection program applied to the tomographic images of Figure 4.3.

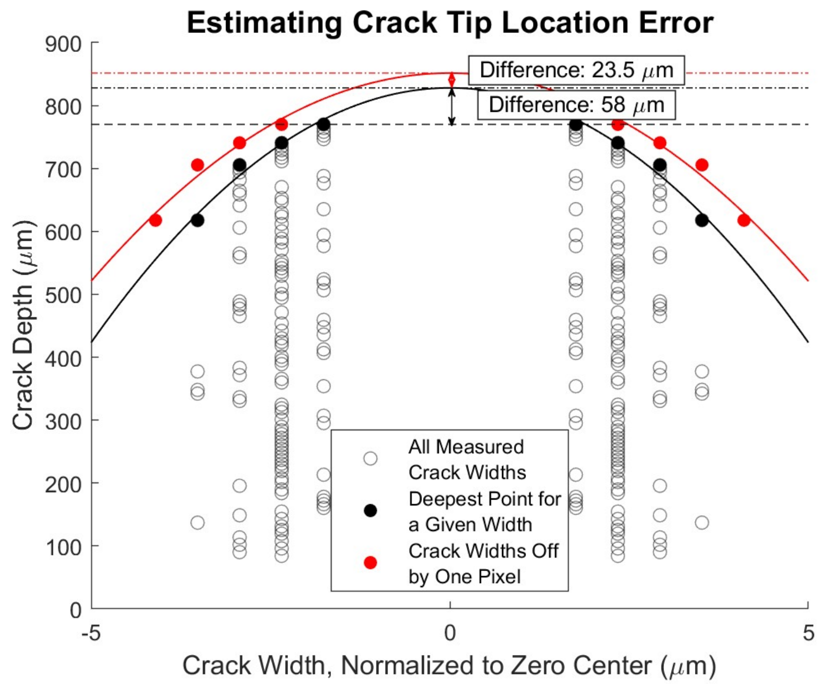

Figure 4.5: Measured crack widths at a sample location with the fitted parabola to the selected best points (black) and the wider points (red). Relevant distances between the intercept of the best points parabola (approximately the deepest point marked by the crack detection program), the deepest point with good resolution, and the intercept of the parabola with 1 pixel uncertainty, are labeled. The average differences when compared at multiple sample locations were 25 and 50 μm.

4.3 Results

4.3.1 FF-HEDM strain tensors

Upon loading, the randomly oriented AlON grains displayed individual strain states, the magnitudes of which varied slightly between different sections of the grain if its volume was captured in multiple FF-HEDM scans. Average strains were generally compressive in the direction of applied load (Figure 4.6a-b), in accordance with the compressive load, while the strains in the orthogonal directions trended more tensile, and had smaller magnitudes (Figure 4.6c-f). With increased loading, the magnitudes of the compressive and tensile strains increased along each primary axis in the reference frame, and the width of the range of the strains tended to increase as well, as a result of each grain having a unique response to the system load.

Additionally, the stress field displayed a dependence on crack location. For grains located under the hole and near the plane of the crack, the stresses in x and z followed roughly the same trend as those further away on the edges of the sample. In the y direction, however, the stress was lower in magnitude for those grains in the path of the crack for approximately 700-800 μm before converging in Sample 1, and 700-1100 μm for Sample 4 (Figure 4.7).

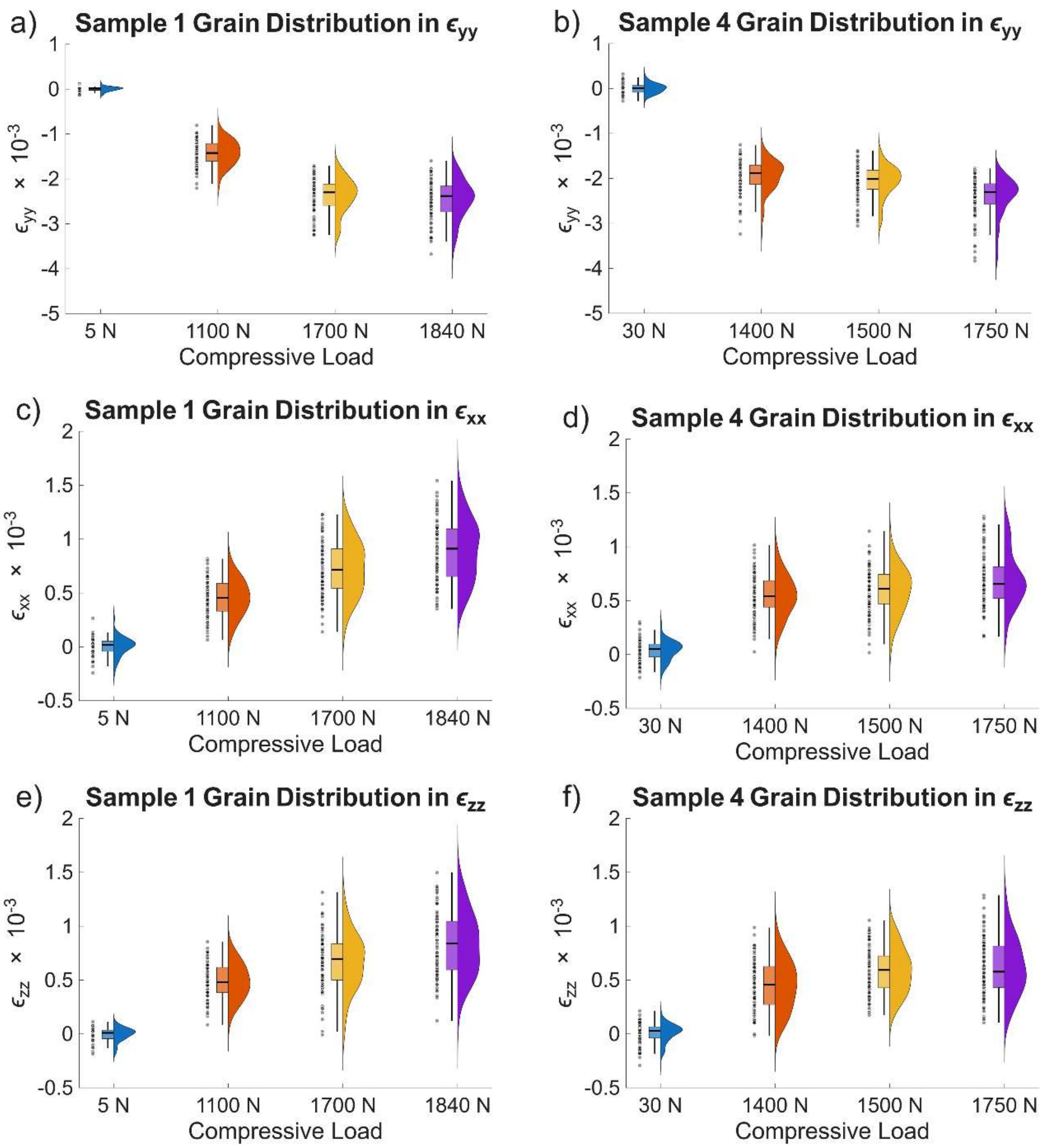

Figure 4.6: Raincloud plots for the strain tensor component at multiple load steps for grains illuminated via FF-HEDM. For each load step, the individual strain values are plotted beside the box plot and density plot to highlight the median value, interquartile range, and distribution. Left (a,c,e): Sample 1 and Right (b,d,f): Sample 4. a-b) ϵ_{yy}, where y is the direction of loading, c-d) ϵ_{xx}, where x is perpendicular to the hole in the sample, and e-f) ϵ_{zz}, where z is directed along the hole.

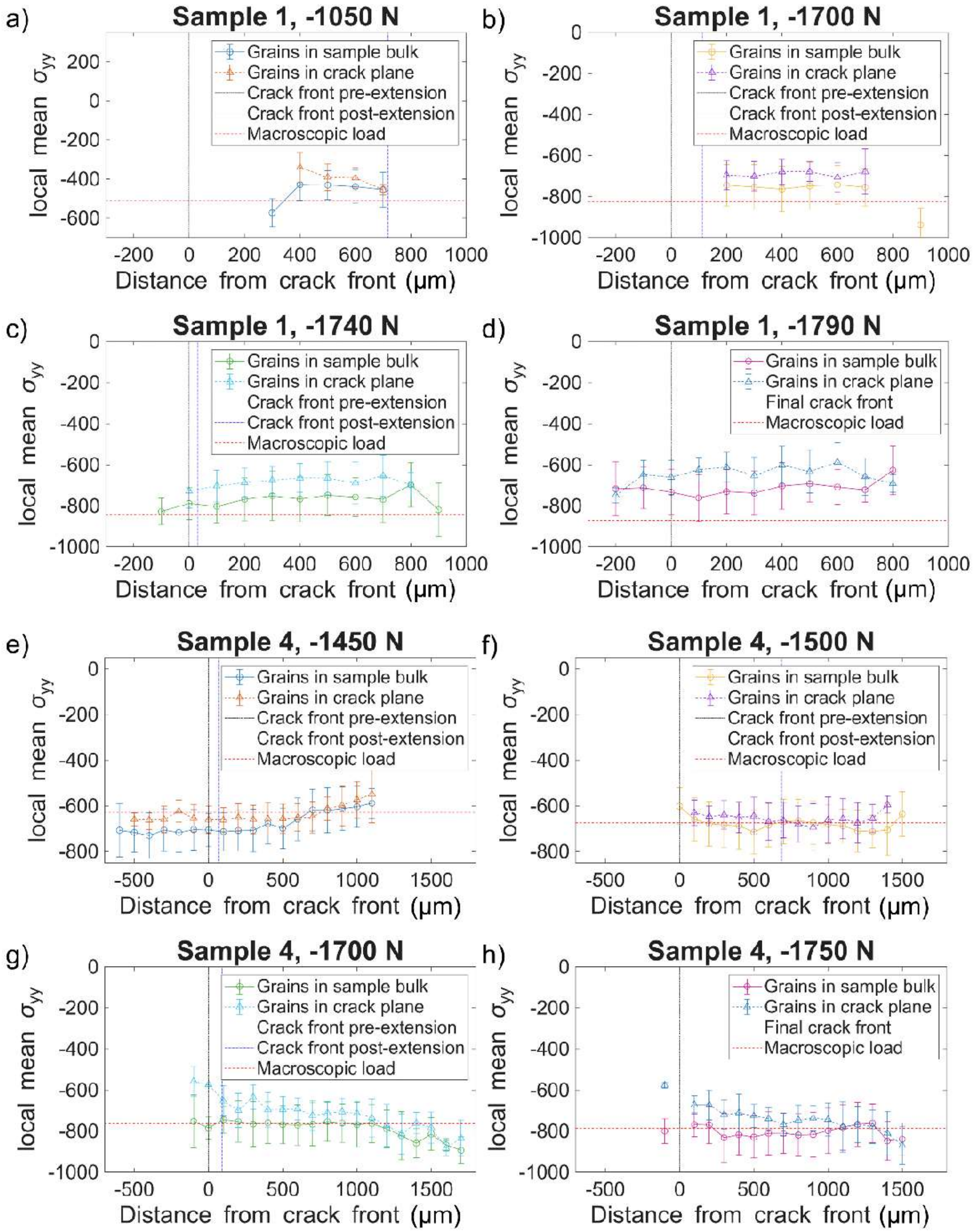

Figure 4.7: The average stresses, determined via FF-HEDM, in the loading (y) direction as a function of distance from the crack front, compared to the macroscopic applied load and with future crack extensions shown. a-d) Sample 1. e-h) Sample 4.

4.3.2 Crack extension

First pop-in on both the upper and lower side of the hole was achieved at -1160 N in Sample 1 and -1536 N in Sample 4 (Figure 4.8a,c,e). After segmentation of the tomography (Figure 4.8b,d), the initial pop-in event in Sample 1 was measured to be about 81 μm at its deepest point, approximately the diameter of a single grain. Sample 4 experienced a larger amount of extension at pop-in, which ended at about 1314 μm at its deepest point, greater than an order of magnitude more than Sample 1. A smaller event may have preceded and been subsumed by this extension, but this was unclear as it was not captured via μ-CT.

In Sample 1, the crack popped in approximately parallel to the hole's center line, with some deviation near the center of the sample (Figure 4.3a). As the crack extended further, while it continued to have some regions where it deviated from the center line, the two-dimensional projection became even more linear (Figure 4.3b), in accordance with expectations laid out in literature for both the DCDC geometry [27] and brittle, microscopically anisotropic materials with macroscopic isotropy [28]. In Sample 4, the popped-in crack was more complex, spanning from the outer edge of the hole on one face towards the center, where it branched into two crack fronts which reached to the edges of the hole on the other side (Figure 4.3c). Further, as the load was increased, another branch popped in at the hole, next to the unbranched section of the original crack, forming close to an X shape with diagonals stretching from the outer edges of the hole on one face to the opposite edges on the other face (Figure 4.3d). Closer to the crack tip, the earlier stages of the crack coalesced into a single crack front, with the 2D projection again much straighter than that just below the hole (Figure 4.3e). However, when the new branch popped in at the hole, it continued to extend until it surpassed the former crack tip, becoming the new singular crack front (Figure 4.3f).

Crack progression continued irregularly in Samples 1 and 4; instead of achieving a stable velocity or growing proportionally to the applied load, the crack in both samples continued to act similarly to the initial growth event. The crack essentially popped-in to each new section in jumps ranging from ~50 μm to over 1 mm, similar to the variance in initial pop-in lengths, and often the extension was localized and may have only extended through a few grains along the crack front at a time. As noted for pop-in, the smallest jumps are around the same size as the smallest grain diameter, indicating that the crack in each region of extension moves across or around one or more discrete grains before being pinned at grain boundaries.

The new extent of the crack and the load at which extension occurred is visualized in Figure 4.8e.

In general, the greatest extension occurred near the center of the sample, similar to the U-shaped curve predicted by Fett et al. [29] and seen by Nielsen et al. in a DCDC polymethylmethacrylate sample [30]. However, the shape of the crack front was far more irregular than modeled by those authors, varied between both samples, and was not self-similar with each further extension (Figure 4.8a,c).

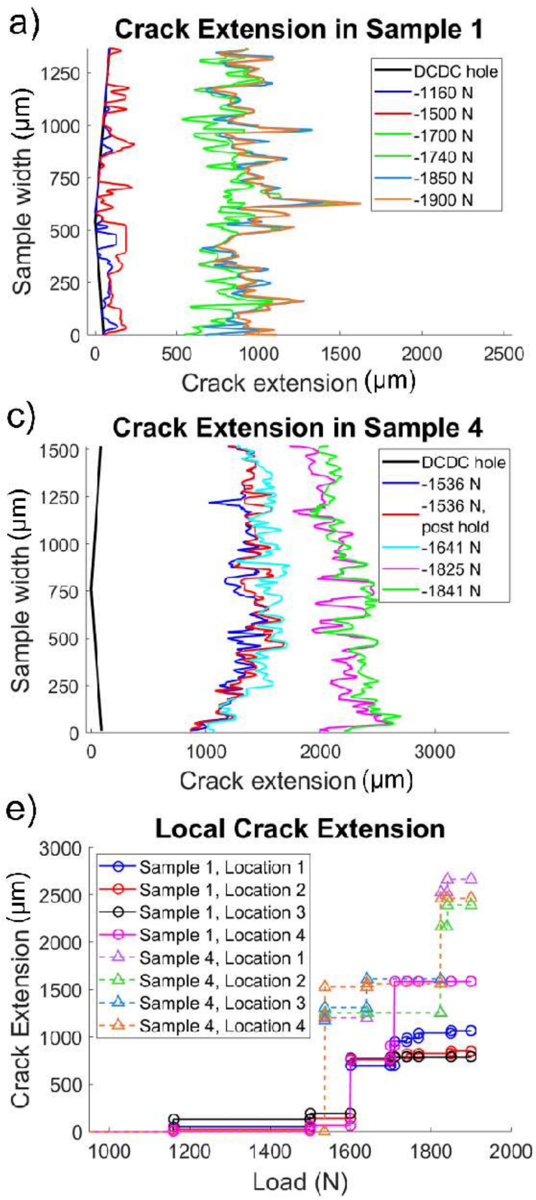

Figure 4.8: Visualization of crack extension. The crack front extended in discrete events as loading increased in both a) Sample 1 and c) Sample 4, although the crack front was not self-similar at each new extent. b) A representative tomographic volume from Sample 1 displaying the hole of the DCDC geometry. d) The pointwise segmented crack from the volume in b) corresponding to the crack front in Sample 1 at -1900 N as seen in a). e) Crack extension as a function of macroscopic load in Samples 1 and 4 at multiple locations along the crack front, showing that the crack front progressed irregularly.

Samples 1 and 4 were loaded to a maximum of -1900 N. The crack grew to a maximum length of 1.71 mm in Sample 1 and 2.51 mm in Sample 4 at the deepest point. As the cracks grew, the opening width at the hole also grew larger. In Sample 1, the opening width at pop-in was smaller than the reliable tomographic resolution and was visible only from the presence of phase-contrast artifacts [26] and can be assumed to be much smaller than 5 μm, but at -1900 N the crack spanned at least 7 μm at its widest. For Sample 4, the opening width after pop-in at -1536 N spanned about 4.7 μm and widened slightly to 5.9 μm at -1900 N.

4.3.3 Intergranular vs transgranular fracture

Grain maps from the limited regions with both FF-HEDM and NF-HEDM are registered with tomographic reconstructions, such that tracking which grains the crack went around or through, and their associated local crystallographic orientation and stress state, is achievable (Figure 4.9a-b). For areas where NF-HEDM confidence was low in between two grains (less than 80%), the crack was considered as being intergranular if it passed through those regions. AlON tends to crack transgranularly [14,31], so grain boundaries are not expected to impact the crack's path significantly, and while face-centered cubic structure, in general and in AlON, often has {111} slip planes [32], the crack was not observed on those planes in particular (Figure 4.9c-d). The average crack plane and its normal were calculated using singular value decomposition on the segmented crack points proximal to that grain.

Grains which were cracked transgranularly or which neighbored an intergranular section of the crack were not clustered around preferred orientations, and the two populations did not display any different trends in orientation (Figure 4.10a). Additionally, the average plane of the crack in those grains did not correspond to any notable cubic slip planes or clusters of planes, indicating there were no preferred or prohibited crack planes (Figure 4.10b). Further, the grains which were cracked transgranularly and those bypassed by intergranular fracture also did not have any differing trends in strain or stress response (as observed before crack extension) when compared to each other or the entire population of grains (Figure 4.10c-d). The stress magnitudes across the crack and in other directions also did not display any correlation to the grain orientations in the full population of grains or the intergranular and transgranular populations (Figure 4.10e-f).

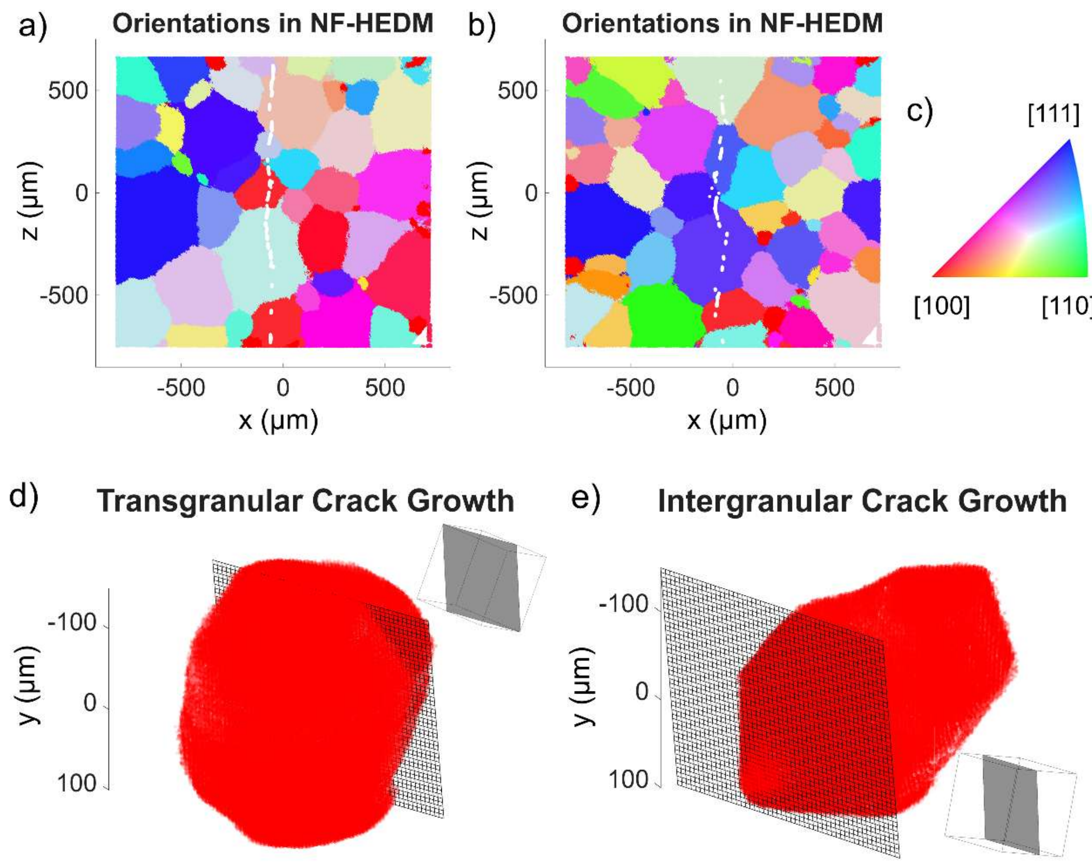

Figure 4.9: Registration of μ-CT and NF-HEDM in Sample 1. a-b) NF-HEDM reconstructed microstructures in x-z slices, 389 μm and 589 μm away from the bottom of the hole respectively. Grain orientations are shown in standard inverse pole figure coloring (c), and the crack extracted from tomography is superimposed in white. NF-HEDM data was collected at -1160 N load, before the crack extended through the region. d) 3D model of a grain which was cracked transgranularly and e) one around which the crack grew intergranularly, with the average crack plane (black mesh) superimposed; insets show the orientation of the crack plane with respect to the grain's unit lattice.

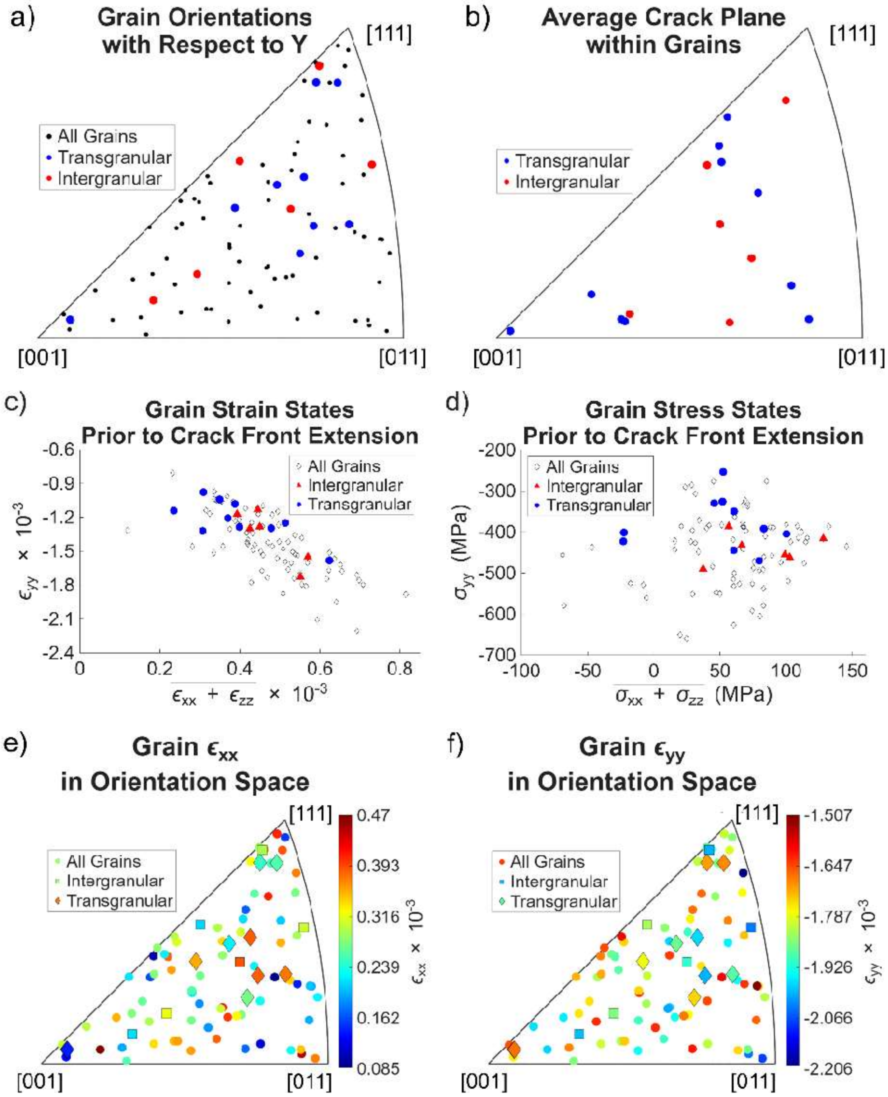

Figure 4.10: FF-HEDM data corresponding to the NF-HEDM volume in Figure 4.9, with the grains through which the crack moved (transgranular) and those which it moved around (intergranular) marked. a) Inverse pole figure for the grain orientation component with respect to the loading direction. b) Orientation distribution of the direction normal to the average plane of the crack within each grain's unit lattice, as visualized in 7c-d). c-d) Distribution of the strain and stress states, respectively, with the component in the loading direction *y* plotted against the average of the two transverse components. e) Distribution of the stress component in *x*, approximately perpendicular to the crack (colors), vs the orientation map in a). f) Distribution of the stress component in *y* (in the loading direction) vs the orientation in a).

4.4 Discussion

4.4.1 Fracture toughness

In Sample 1, crack extension only occurred with increased load beyond the load at previous extension, in accordance with the DCDC geometry expectation. However, the crack did not extend with every increase in load, instead becoming arrested even as the load increased by hundreds of Newtons. Sample 4 behaved similarly after pop-in for its first few extensions, although the initial crack had some branching and the lengthier initial pop-in indicates some initial instability. Further, the second pop-in event and subsequent new location of the crack tip (Figure 4.3e-f) indicates that it became more favorable to pop-in a new crack front rather than extend the original front segment further.

Prior to the second pop-in, a localized gradient in σ_{yy} was observed ahead of the crack front (Figure 4.7g). Before the new pop-in, the compressive stress experienced by the volume just ahead of the crack decreased when compared to the volume away from the crack, while at distances far from the crack, the magnitude was greater than the applied load. While the limited number of discrete extension events precludes a definitive statistical correlation, this observation suggests that localized stress heterogeneities play a role in intermittent crack propagation as the stresses acting to open and extend the crack become disrupted [33].

We are currently working to explore such considerations in anisotropic and polycrystalline media using dedicated phase-field models, as well as to relate stress development and crack motion to differently oriented lattice planes and grain boundaries. These local microstructural changes can provide further barriers to unimpeded growth as the energy needed to extend cracks in these regions changes due to the anisotropic elastic constants. In a related work to this thesis, when systematically studying crack behavior at grain boundaries based on FF-HEDM data as a function of the five grain boundary degrees of freedom, both the misorientation and the plane normal direction are identified as important for crack pinning [34].

The large crack extension events such as at the initial and secondary pop-ins in Sample 4 and the jump at -1600 N in Sample 1 indicate that there are also regions where crack growth is relatively uninhibited. In an isotropic sample with invariant fracture toughness, the incremental increase in load needed to induce cracking in the next region grows proportionally with crack length [35]. Here in the anisotropic samples, that load requirement is additionally affected by the local fracture toughness, and the necessary load may be increased (leading to the crack becoming arrested as greater loading is needed to extend it) or reduced (causing longer extension events). If the crack front was arrested at a region with higher fracture toughness, and subsequently grows after the load is increased, it may enter a region where the necessary load to extend the crack has already been exceeded, and thus it will proceed until reaching another stopping point. The changing fracture toughnesses in differently oriented grains can be seen in the work of Guo et al. in [32], where the average measured fracture toughness range is reported as well as the fracture toughnesses measured for two individual grains, which are both outside that average.

From the literature, the fracture toughness (K_{Ic}) of AlON has an average value of 2.09 ± 0.06 MPa $\sqrt{\mathrm{m}}$ [31] using the single-edge pre-cracked beam geometry in air. Other methods, including the single-edge pre-notched beam geometry [36] and Berkovich nanoindentation [32], result in average values ranging from 2.4 to 3 MPa $\sqrt{\mathrm{m}}$; however, outliers from the latter had values measured as low as 1.4 MPa $\sqrt{\mathrm{m}}$. These values are reported against those from this work, obtained using Equation 2.5 [37].

Crack extension in Sample 1 occurred at higher loads relative to crack length than Sample 4 for all growth events, and thus had higher fracture toughness values, which fell within the range reported from the single-edge pre-notched beam geometry and Berkovich nanoindentation. This effect may be partially explained by the fact that the compressive y stress ahead of the crack in Sample 1 was in general lower in magnitude than the applied stress, and thus higher loads were needed to reach the equivalent stress for local extension (Figure 4.7). Meanwhile, the fracture toughness of Sample 4 was in the lower range obtained from the single-edge pre-cracked beam geometry (Figure 4.11). The earliest extension events in Sample 1 were not included, as the relative length of the crack front did not satisfy the $\beta \leq \alpha$ condition required in Equation 1.

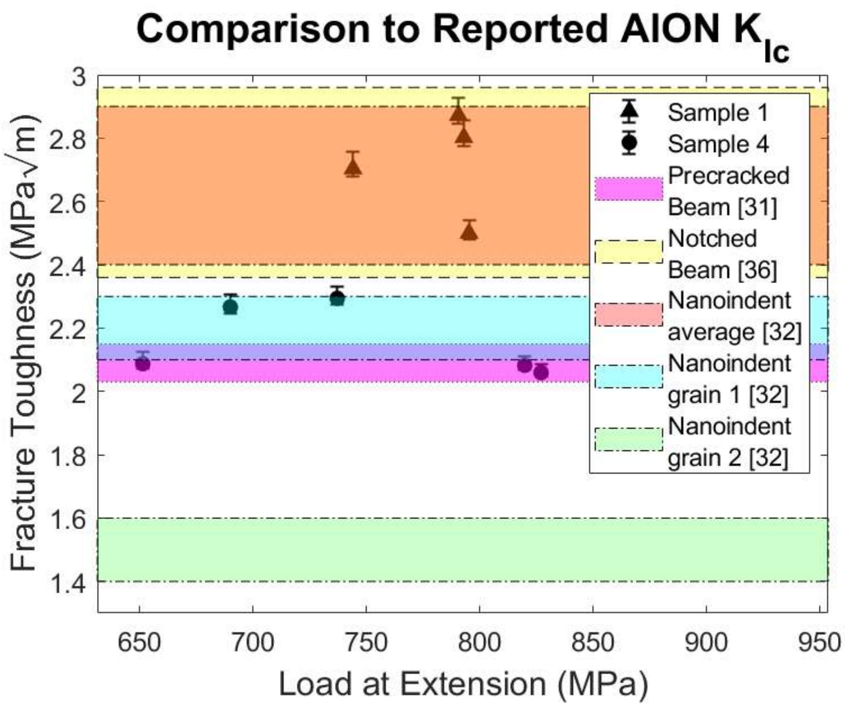

Figure 4.11: The calculated fracture toughness using Equation 2.5 from reference [37] compared to the isotropic fracture toughness of aluminum oxynitride (AlON), using the maximum crack length, and the RAMS load at which crack extension occurred. Data points from Samples 1 and 4 are plotted against the reported ranges of AlON from the precracked beam test [31], the average range and two individual grain ranges from Berkovich nanoindentation [32], and the notched beam test of reference [36] and one of the individual grain measurements [32].

4.4.2 Intragranular strain variation

Individual AlON grains have not only different fracture toughnesses varying with orientation [32] but also a spread in that measurement, indicating that the strain field varies within grains and further complicating the microstructure with which the growing crack front interacts. This is corroborated by the fact that for grains with diameters larger than the 100 μm height of the FF-HEDM scans, the average reported strain tensor could vary by $1\text{-}3\times10^{-4}$ in different regions that were illuminated by the beam. Additionally, within many grains mapped via NF-HEDM, the completeness value can vary, indicating regions of greater and lesser agreement with the expected diffraction pattern. The altered confidence could be a result of variations in the chemical composition of AlON, especially in the local ratio of oxygen to nitrogen, which is correlated with lattice parameter [14]. Narrow twinned regions with widths on the order of a few microns have also been reported in AlON [38], and might provide a source of lowered confidence.

Taken together, the variation in average strain tensor and diffraction pattern for different sub-granular regions indicates that the imposed macroscopic load is distributed unevenly among grains as a result of the grains' anisotropy and differing size and orientation. Cocke et al. have performed analysis based on the samples in this work, aiming to recover the intragranular strain fields and spatially resolved macrostress state from the grain-averaged data, with simulations demonstrating high stress variance spatially within grains [39].

4.4.3 Microstructural effects on crack behavior

While it appears that the orientation, stress, and strain of the grains ahead of the crack has little effect on whether the crack moves transgranularly or intergranularly, this is not to say that there is no effect of these variables on the crack itself. As already shown, grain orientation can have a major effect on the local fracture toughness, and the stress and strain states of adjacent grains necessarily impact each other, all of which taken together play a major role in where the crack front stops after extending.

As noted earlier, in the literature AlON does tend to crack transgranularly, indicating that the grain boundaries do not have such a lower fracture toughness compared to the grains that they would sharply alter the crack path. While the crack did change orientation as it grew, angular changes were usually gradual, smooth, and occurred over a range of tens to hundreds of microns, that is, over the range of grain sizes in the AlON studied. With few persistent orientation changes in the form of a sharp angle beyond those angles inherited from the shape of the popped-in crack, or deflections of entire grain-size segments of the crack, the crack often retained much the same orientation when entering a grain below its position instead of having its path altered to go around a grain. Partly, this may be the case due to the size of the grains. Creating surface area around a grain with a diameter of 100 μm or more would be energetically costly, and the crack's arrest and persistent shape upon further extension shows that it is generally more favorable for the energy to be released by eventual extension rather than immediate deflection to a grain boundary not in the vicinity of the crack. While grains which were adjacent to intergranular cracks generally had larger radii, there were also transgranularly-cracked grains with similar radii, so radius alone is not an indicator of whether a grain will be cleaved by fracture. However, a more salient point is that most of the intergranularly-cracked grains were more distant from the center of the sample than the transgranularly-cracked grains, and notably, the intergranular grains' radii were larger than that distance, indicating that those grains did not cross the center plane of the sample, while the transgranular grains did, and were thus closer to the direct path of the crack (Figure 4.12).

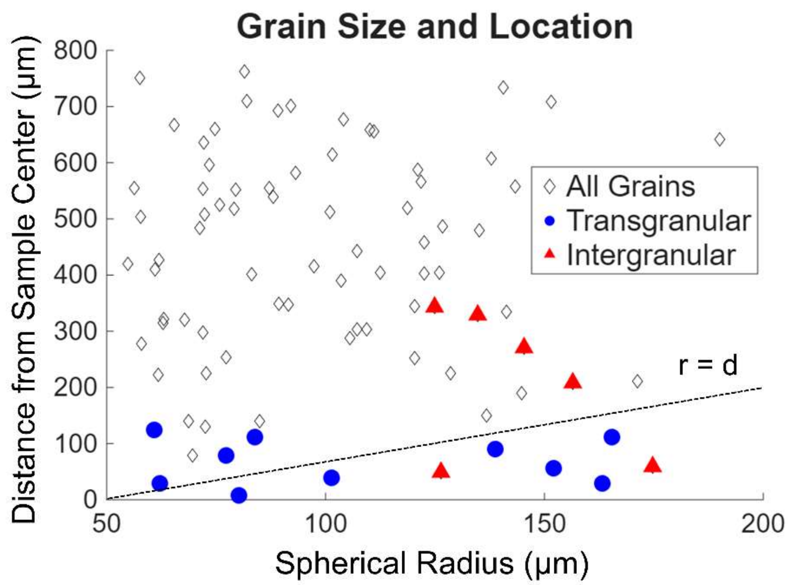

Figure 4.12: Radius of AlON grains versus the distance between their centers of mass and the center plane of the DCDC sample, with unity marked.

In addition to the gradual changes related to grain boundaries, there are smaller deflections present; most of these orientation changes occur over a range of a few to ten or so microns, and then straighten out again. Based on the fact that the crack does not sharply change its orientation to go around large grains, these deflections are presumed to occur near grain boundaries the crack is already growing near. Additional causes of deflection include rare pores, which have a fracture toughness of zero and are therefore preferential to pass through (Figure 4.13). Finally, the crack occasionally changes direction within grains, potentially corresponding to stacking twinning faults not detected as a change in grain orientation by the techniques used, but also likely as part of the gradual angular changes induced by the microstructure ahead of the crack. Previous work has identified deflections when encountering both grain and twin boundaries, which often result in the crack kinking over the span of a few microns or less before continuing to grow in much the same direction and orientation as previously [38]. Some jaggedness and kinking are indeed visible in the crack in the tomography images (Figure 4.13), although at the scale of a micron or smaller this effect is at the spatial resolution limit and the size of the kink is subject to error. A similar effect can be seen at a grain boundary in Sample 1 (Figure 4.14), although the overall angle of the crack does not change overmuch. Notably, the crack plane is nearly parallel to the {100} direction in the first grain's unit lattice, which might have served as an attractive plane on which the crack could propagate. The degree of change between two different atomic arrangements could result in the crack being impeded from remaining on a single plane through both grains but the considerations above, the crack's tendency to become straighter as it extends deeper, and its speed when extending might have contributed to the crack maintaining a similar angle in both grains.

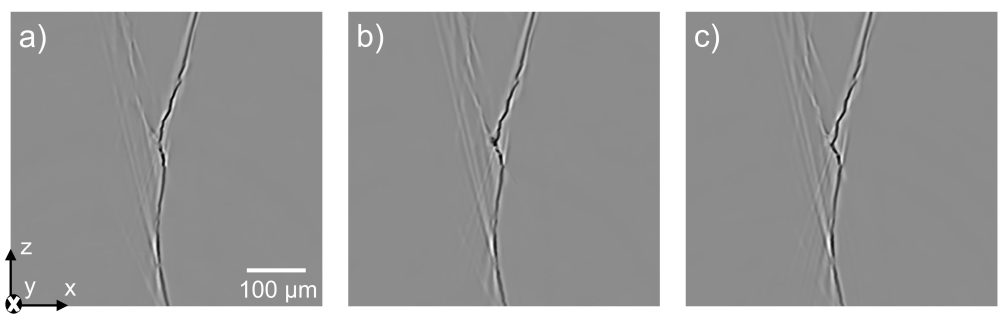

l_{crack} = 1.406 mm l_{crack} = 1.412 mm l_{crack} = 1.418 mm

Figure 4.13: A pore interacting with the crack front (dark line) in Sample 4. The white streaks on the left side are wrinkle artifacts. a) Above the pore in the loading direction y, the crack has a mostly smooth curve with some jagged edges. b) The crack deflects to intersect the pore. c) After leaving the pore, the crack retains the sharp kink. Also visible near the deflection are changes in the crack direction between two orientations which are smaller than the diameter of a single grain, potentially indicating the crack is crossing twinning faults or other crystal discontinuities.

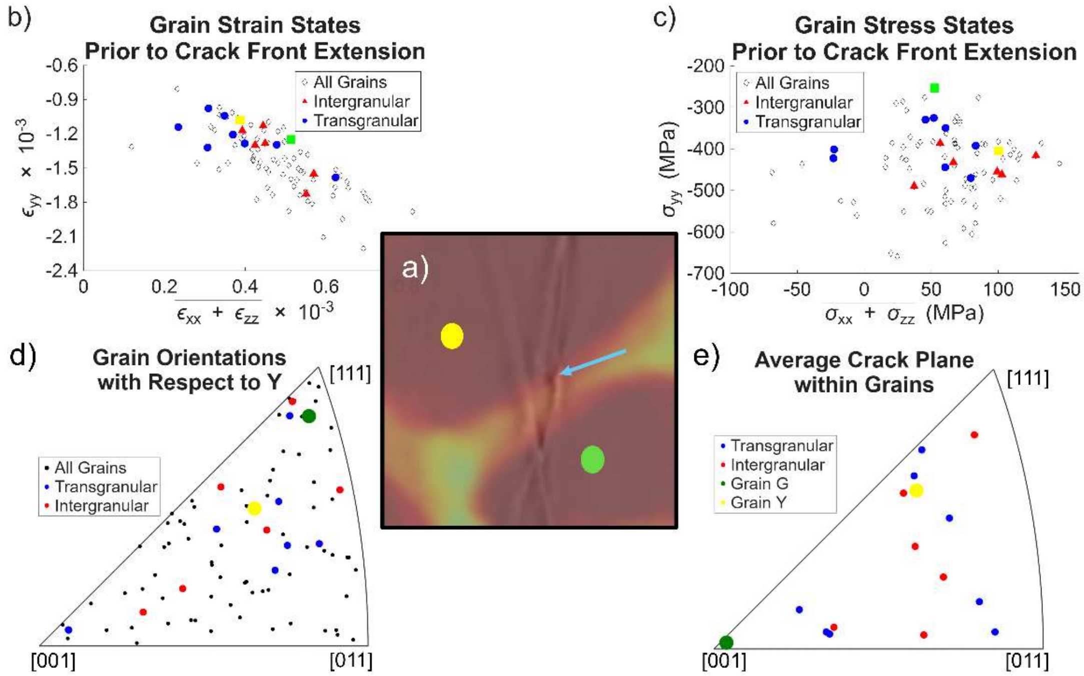

Figure 4.14: A kink at a grain boundary in Sample 1. a) Grain Y (yellow) and grain G (green) are both intersected transgranularly by the crack, but at the grain boundary, the crack gains a sharp kink (blue arrow). b-c) The values of strain and stress from Figure 4.10c-d), with the values for grains Y and G highlighted. d) The orientations of grains Y and G highlighted within the distribution from Figure 4.10a). e) The orientation of the crack normal within grains Y and G highlighted within the distribution from Figure 4.10b).

4.5 Conclusions

We have demonstrated that visualizing brittle fracture of a polycrystalline ceramic at multiple extension steps is possible using the DCDC geometry and the precise loading of RAMS-III fixture at the Advanced Photon Source. The information presented here demonstrates that this study's 3D, in-situ monitoring of a growing crack is superior to 2D and postmortem studies in capturing microstructural and stress-induced changes, including retardations in the crack's growth. We have shown that a 3D, growing crack can be complex, with an uneven crack front impacted by the microstructure ahead of the crack tip, the grain orientation, and the position of grain boundaries. Additionally, the high tomographic resolution of the crack's shape throughout the material and the registry of that shape to NF-HEDM scans are valuable pieces of information for phase-field modelers and others performing computations seeking to describe the exact mechanisms affecting the crack's shape, length, and growth rate.

For AlON specifically, we have shown that the crack front extends in multiple pop-in-like events which may span a distance equivalent to a single grain along the crack front or many grains along its entire length. Further, additional pop-in events at the hole are possible, which may create a new crack front in a more favorable region for extending, and it may eventually surpass the original crack front. While the crack grows both intergranularly along grain boundaries and transgranularly with no preferred lattice planes, it may experience deflections in its orientation at grain boundaries and potentially at twinning faults. However, the grains through which the crack grew transgranularly and those beside which it grew intergranularly have no distinguishable or differing trends in orientation or stress state; rather, the grain only grew along grain boundaries when it was proximal to them while extending. Instead, the greater factor controlling growth is the changing fracture toughness of the region ahead of the crack as it encounters grains of different orientations. In regions of greater fracture toughness, the extension of the crack front is arrested until the load is increased sufficiently, after which it grows through regions of lower fracture toughness until its motion is again halted.

The information gathered from this work is extremely pertinent to building and verifying the above-mentioned phase-field models. Current collaborations have already produced results demonstrating crack pinning as observed in these experiments, and related pinning to the degrees of freedom of grain boundaries [34]. By selecting grain boundaries with singularity exponents that lead to crack pinning and computing the singularity in the stress for a crack tip at various grain boundaries, a corresponding increase in resistance to crack propagation is observed. In the future, we will be applying these insights to the experimental dataset to evaluate the performance of the model.

Future experimental work could be performed on anisotropic brittle materials with smaller grains in order to increase the number of grain boundaries, orientations, and stress states with which the crack interacts. By using materials with different crystal structures and degrees of anisotropy, trends not present in AlON might be uncovered. Further, recently-developed 2D scanning FF-HEDM using a point-focused beam, rather than the 1D scanning performed here [40], could be used to resolve intragranular strain fields and better reveal the nature of the strain tensor ahead of the crack as well as any local changes within a grain which might cause it to kink or change orientation.

Acknowledgments

This work was sponsored by the US Office of Naval Research Grant No. N00014-21-1-2784. SFG was also supported by the US National Science Foundation Graduate Research Fellowship No. 2139433. Additionally, the authors would like to thank Dr. Paul Shade and the Air Force Research Laboratory for the generous use of RAMS-III. This research was performed on APS beam time award from the Advanced Photon Source, a U.S. Department of Energy (DOE) Office of Science user facility operated for the DOE Office of Science by Argonne National Laboratory under Contract No. DE-AC02-06CH11357.

Bibliography

[1] R.W. Armstrong, The influence of polycrystal grain size on several mechanical properties of materials, *Metall Trans* 1 (1970) 1169–1176. https://doi.org/10.1007/BF02900227.

[2] H.D. Espinosa, P.D. Zavattieri, A grain level model for the study of failure initiation and evolution in polycrystalline brittle materials. Part I: Theory and numerical implementation, *Mech Mater* 35 (2003) 333–364. https://doi.org/10.1016/S0167-6636(02)00285-5.

[3] N. Hansen, X. Huang, Microstructure and flow stress of polycrystals and single crystals, *Acta Mater* 46 (1998) 1827–1836. https://doi.org/10.1016/S1359-6454(97)00365-0.

[4] B. Chen, J.N. Hu, Y.Q. Wang, S.Y. Zhang, S. Van Petegem, A.C.F. Cocks, D.J. Smith, P.E.J. Flewitt, Role of the misfit stress between grains in the Bauschinger effect for a polycrystalline material, *Acta Mater* 85 (2015) 229–242. https://doi.org/10.1016/j.actamat.2014.11.021.

[5] T.J. Stannard, J.J. Williams, S.S. Singh, A.S. Sundaram Singaravelu, X. Xiao, N. Chawla, 3D time-resolved observations of corrosion and corrosion-fatigue crack initiation and growth in peak-aged Al 7075 using synchrotron X-ray tomography, *Corros Sci* 138 (2018) 340–352. https://doi.org/10.1016/j.corsci.2018.04.029.

[6] S.E. Gustafson, D.C. Pagan, P.A. Shade, M.D. Sangid, Dynamic recovery observed in distinct grains within a polycrystalline nickel-based superalloy during cyclic high temperature fatigue via high energy X-ray diffraction microscopy, *Scripta Mater* 192 (2021) 37–42. https://doi.org/10.1016/j.scriptamat.2020.10.004.

[7] J.V. Gordon, R.E. Lim, M.J. Wilkin, D.C. Pagan, R.A. Lebensohn, A.D. Rollett, Evaluating the grain-scale deformation behavior of a single-phase FCC high entropy alloy using synchrotron high energy diffraction microscopy, *Acta Mater* 215 (2021) 117120. https://doi.org/10.1016/j.actamat.2021.117120.

[8] W. Chen, J. Xu, C. Ding, D. Shan, B. Guo, T.G. Langdon, Fracture mechanism of electrically-assisted micro-tension in nanostructured titanium using synchrotron radiation X-ray tomography, *Scripta Mater* 222 (2023) 114997. https://doi.org/10.1016/j.scriptamat.2022.114997.

[9] H.R. Sandgren, Y. Zhai, D.A. Lados, P.A. Shade, J.C. Schuren, M.A. Groeber, P. Kenesei, A.G. Gavras, Characterization of fatigue crack growth behavior in LENS fabricated Ti-6Al-4V using high-energy synchrotron x-ray microtomography, *Addit Manuf* 12 (2016) 132–141. https://doi.org/10.1016/j.addma.2016.09.002.

[10] D.P. Naragani, P.A. Shade, P. Kenesei, H. Sharma, M.D. Sangid, X-ray characterization of the micromechanical response ahead of a propagating small fatigue crack in a Ni-based superalloy, *Acta Mater* 179 (2019) 342–359. https://doi.org/10.1016/j.actamat.2019.08.005.

[11] A.D. Spear, S.F. Li, J.F. Lind, R.M. Suter, A.R. Ingraffea, Three-dimensional characterization of microstructurally small fatigue-crack evolution using quantitative fractography combined with post-mortem X-ray tomography and high-energy X-ray diffraction microscopy, *Acta Mater* 76 (2014) 413–424. https://doi.org/10.1016/j.actamat.2014.05.021.

[12] M. Herbig, A. King, P. Reischig, H. Proudhon, E.M. Lauridsen, J. Marrow, J.-Y. Buffière, W. Ludwig, 3-D growth of a short fatigue crack within a polycrystalline

microstructure studied using combined diffraction and phase-contrast X-ray tomography, *Acta Mater* 59 (2011) 590–601. https://doi.org/10.1016/j.actamat.2010.09.063.
[13] M.B. Cil, K.A. Alshibli, P. Kenesei, 3D Experimental Measurement of Lattice Strain and Fracture Behavior of Sand Particles Using Synchrotron X-Ray Diffraction and Tomography, *J Geotech Geoenviron* 143 (2017) 04017048. https://doi.org/10.1061/(ASCE)GT.1943-5606.0001737.
[14] J.W. McCauley, P. Patel, M. Chen, G. Gilde, E. Strassburger, B. Paliwal, K.T. Ramesh, D.P. Dandekar, AlON: A brief history of its emergence and evolution, *J Eur Ceram Soc* 29 (2009) 223–236. https://doi.org/10.1016/j.jeurceramsoc.2008.03.046.
[15] N.D. Corbin, Aluminum oxynitride spinel: A review, *J Eur Ceram Soc* 5 (1989) 143–154. https://doi.org/10.1016/0955-2219(89)90030-7.
[16] P.A. Shade, B. Blank, J.C. Schuren, T.J. Turner, P. Kenesei, K. Goetze, R.M. Suter, J.V. Bernier, S.F. Li, J. Lind, U. Lienert, J. Almer, A rotational and axial motion system load frame insert for in situ high energy x-ray studies, *Rev Sci Instrum* 86 (2015) 093902. https://doi.org/10.1063/1.4927855.
[17] H. Sharma, R.M. Huizenga, S.E. Offerman, A fast methodology to determine the characteristics of thousands of grains using three-dimensional X-ray diffraction. I. Overlapping diffraction peaks and parameters of the experimental setup, *J Appl Cryst* 45 (2012) 693–704. https://doi.org/10.1107/S0021889812025563.
[18] H. Sharma, R.M. Huizenga, S.E. Offerman, A fast methodology to determine the characteristics of thousands of grains using three-dimensional X-ray diffraction. II. Volume, centre-of-mass position, crystallographic orientation and strain state of grains, *J Appl Cryst* 45 (2012) 705–718. https://doi.org/10.1107/S0021889812025599.
[19] H. Sharma, marinerhemant/MIDAS, (2025). https://github.com/marinerhemant/MIDAS (accessed January 12, 2026).
[20] S. Satapathy, M. Ahart, D. Dandekar, R.J. Hemley, B. Schuster, P. Khoma, Single-Crystal Elastic Properties of Aluminum Oxynitride (AlON) from Brillouin Scattering, *J Amer Ceram Soc* 99 (2016) 1383–1389. https://doi.org/10.1111/jace.14065.
[21] S.D. Shastri, J. Almer, C. Ribbing, B. Cederström, High-energy X-ray optics with silicon saw-tooth refractive lenses, *J Synchrotron Rad* 14 (2007) 204–211. https://doi.org/10.1107/S0909049507003962.
[22] S.D. Shastri, P. Kenesei, A. Mashayekhi, P.A. Shade, Focusing with saw-tooth refractive lenses at a high-energy X-ray beamline, *J Synchrotron Rad* 27 (2020) 590–598. https://doi.org/10.1107/S1600577520003665.
[23] B.A. Dowd, G.H. Campbell, R.B. Marr, V.V. Nagarkar, S.V. Tipnis, L. Axe, D.P. Siddons, Developments in synchrotron x-ray computed microtomography at the National Synchrotron Light Source, in: Developments in X-Ray Tomography II, SPIE, 1999: pp. 224–236. https://doi.org/10.1117/12.363725.
[24] A. Buades, B. Coll, J.-M. Morel, Non-local means denoising, *Image Processing On Line* 1 (2011) 208–212. https://doi.org/10.5201/ipol.2011.bcm_nlm.
[25] Continuum aspects of crack propagation I: linear elastic crack-tip field, in: Fracture of Brittle Solids, 2nd ed., Cambridge University Press, Cambridge, 1993: pp. 16–50. https://doi.org/10.1017/CBO9780511623127.
[26] C. Xiao, J.-Y. Buffière, J.M. Létang, W. Ludwig, Investigation of wrinkle artifacts along metallic fatigue cracks in phase contrast synchrotron tomography via simulations and

experiments, *Mater Charact* 194 (2022) 112431. https://doi.org/10.1016/j.matchar.2022.112431.
[27] J.K. Kurihara, T. Tomimatsu, Y.F. Liu, S.Q. Guo, Y. Kagawa, Mode I fracture toughness of SiC particle-dispersed ZrB2 matrix composite measured using DCDC specimen, *Ceram Int* 36 (2010) 381–384. https://doi.org/10.1016/j.ceramint.2009.07.031.
[28] B. Cotterell, On brittle fracture paths, *Int J Fract* 1 (1965) 96–103. https://doi.org/10.1007/BF00186747.
[29] T. Fett, G. Rizzi, J.P. Guin, J.M. López-Cepero, S.M. Wiederhorn, A fracture mechanics analysis of the double cleavage drilled compression test specimen, *Eng Fract Mech* 76 (2009) 921–934. https://doi.org/10.1016/j.engfracmech.2008.12.016.
[30] C. Nielsen, A.V. Amirkhizi, S. Nemat-Nasser, The effect of geometry on fracture strength measurement using DCDC samples, *Eng Fract Mech* 91 (2012) 1–13. https://doi.org/10.1016/j.engfracmech.2012.04.030.
[31] J.A. Salem, Crack Growth Testing of an Aluminum Oxynitride (AlON) for International Space Station Kick Panes, 2017. https://ntrs.nasa.gov/citations/20170001289 (accessed May 31, 2025).
[32] J.J. Guo, K. Wang, T. Fujita, J.W. McCauley, J.P. Singh, M.W. Chen, Nanoindentation characterization of deformation and failure of aluminum oxynitride, *Acta Mater 59* (2011) 1671–1679. https://doi.org/10.1016/j.actamat.2010.11.034.
[33] T.A. Michalske, W.L. Smith, E.P. Chen, Stress intensity calibration for the double cleavage drilled compression specimen, *Eng Fract Mech* 45 (1993) 637–642. https://doi.org/10.1016/0013-7944(93)90269-X.
[34] M. Ramesh, Phase-Field Modeling of Fracture in Heterogeneous Materials: A Microstructure Sensitive Approach, Northwestern University, 2025.
[35] M.Y. He, M.R. Turner, A.G. Evans, Analysis of the double cleavage drilled compression specimen for interface fracture energy measurements over a range of mode mixities, *Acta Metall Mater* 43 (1995) 3453–3458. https://doi.org/10.1016/0956-7151(95)00036-U.
[36] H.X. Willems, P.F. Van Hal, G. De With, R. Metselaar, Mechanical properties of γ-aluminium oxynitride, *J Mater Sci* 28 (1993) 6185–6189. https://doi.org/10.1007/BF00365041.
[37] Q.Z. Wang, M. Ni, L.Z. Wu, R.Q. Huang, Scrutinized and revised stress intensity factor formulas for double cleavage drilled compression specimens, *Theor Appl Fract Mec* 96 (2018) 803–810. https://doi.org/10.1016/j.tafmec.2017.11.008.
[38] M. Ding, T. Wang, B. Maerz, S. Robertson, Z. Sun, L. Fan, Y. Shi, H. Wu, Formation of twins in AlON material and its effects on the Vickers hardness and fracture toughness, *Ceram Int* 45 (2019) 21127–21135. https://doi.org/10.1016/j.ceramint.2019.07.089.
[39] C.K. Cocke, A. Akerson, S.F. Gorske, K.T. Faber, K. Bhattacharya, On recovering intragranular strain fields from grain-averaged strains obtained by high-energy X-ray diffraction microscopy, *Math Mech Solids* 31 (2026) 122–139. https://doi.org/10.1177/10812865251376693.
[40] W. Li, H. Sharma, P. Kenesei, S. Ravi, H. Sehitoglu, A. Bucsek, Resolving intragranular stress fields in plastically deformed titanium using point-focused high-energy diffraction microscopy, *J Mater Res* 38 (2023) 165–178. https://doi.org/10.1557/s43578-022-00873-y.